Industrial Chemistry & Materials

ROYAL SOCIETY OF CHEMISTRY

PAPER

View Article Online
View Journal | View Issue

Open Access Article. Published on 20 mis Hwevrer 2024. Downloaded on 08/01/2026 10:34:26.
This article is licensed under a Creative Commons Attribution-NonCommercial 3.0 Unported Licence.

Check for updates

Cite this: *Ind. Chem. Mater.*, 2024, **2**, 432

Triphase photocatalytic water-gas-shift reaction for hydrogen production with enhanced interfacial diffusion at gas–liquid–solid interfaces†

Huige Chen,[ab] Zhenhua Li,[a] Chao Zhou, [a] Run Shi *[a] and Tierui Zhang *[ab]

Received 28th December 2023,
Accepted 19th February 2024

DOI: 10.1039/d3im00135k

rsc.li/icm

The exothermic characteristic of the water-gas-shift (WGS) reaction, coupled with the thermodynamic constraints at elevated temperatures, has spurred a research inclination towards conducting the WGS reaction at reduced temperatures. Nonetheless, the challenge of achieving efficient mass transfer between gaseous CO and liquid H_2O at the photocatalytic interface under mild reaction conditions hinders the advancement of the photocatalytic WGS reaction. In this study, we introduce a gas–liquid–solid triphase photocatalytic WGS reaction system. This system facilitates swift transportation of gaseous CO to the photocatalyst's surface while ensuring a consistent water supply. Among various metal-loaded TiO_2 photocatalysts, Rh/TiO_2 nanoparticles positioned at the triphase interface demonstrated an impressive H_2 production rate of 27.60 mmol g^{-1} h^{-1}. This rate is roughly 2 and 10 times greater than that observed in the liquid–solid and gas–solid diphase systems. Additionally, finite element simulations indicate that the concentrations of CO and H_2O at the gas–liquid–solid interface remain stable. This suggests that the triphase interface establishes a conducive microenvironment with sufficient CO and H_2O supply to the surface of photocatalysts. These insights offer a foundational approach to enhance the interfacial mass transfer of gaseous CO and liquid H_2O, thereby optimizing the photocatalytic WGS reaction's efficiency.

Keywords: Water-gas-shift; Photocatalysis; Triphase interface; Hydrogen evolution; TiO_2.

1 Introduction

Hydrogen (H_2) stands as a pivotal renewable chemical with extensive applications in contemporary society.[1–3] Currently, the predominant method for H_2 production involves the steam reforming of hydrocarbons derived from fossil fuels.[4,5] Nevertheless, this steam reforming technique demands elevated temperatures and pressures, leading to substantial costs and energy expenditures. Furthermore, the H_2 generated often retains elevated levels of CO, rendering it less suitable for subsequent industrial applications.[5]

The water-gas-shift (WGS) reaction ($CO + H_2O \rightarrow CO_2 + H_2$) holds significant importance in the chemical industry, serving multiple functions such as H_2 production, CO removal, and syngas adjustment.[6–8] Over recent decades, considerable research has centered on the thermocatalytic WGS reaction.[9–12] Typically, thermocatalytic WGS transpires at temperatures ranging from 180–230 °C for noble metal catalysts, while non-precious metal catalysts necessitate even higher temperatures, surpassing 270 °C.[9,13–16] Nonetheless, the reaction's exothermic nature coupled with thermodynamic constraints at elevated temperatures has spurred increased exploration into the WGS reaction at lower temperatures.

Photocatalysis has garnered extensive attention across various chemical reactions, presenting numerous advantages over conventional thermocatalysis. A primary advantage of photocatalysis lies in its mild reaction conditions and reduced reliance on fossil fuels, as it directly utilizes solar energy to drive reactions.[17,18] Utilizing metal oxide semiconductors like TiO_2, CuO_x, among others, in photocatalysis offers a compelling approach to lowering the WGS reaction temperature to ambient levels.[19,20]

Presently, the photocatalytic WGS reaction predominantly operates within a gas–solid (G–S) diphase system, employing gaseous CO and water vapor as reactants.[19,21] However, at lower temperatures, the constrained saturated vapor pressure of water can impede its interfacial mass transfer, potentially becoming the rate-determining step. Furthermore, water molecules interconnected *via* hydrogen bonds exhibit

[a] *Key Laboratory of Photochemical Conversion and Optoelectronic Materials, Technical Institute of Physics and Chemistry, Chinese Academy of Sciences, Beijing 100190, China. E-mail: shirun@mail.ipc.ac.cn, tierui@mail.ipc.ac.cn*
[b] *Center of Materials Science and Optoelectronics Engineering, University of Chinese Academy of Sciences, Beijing 100049, China*

† Electronic supplementary information (ESI) available. See DOI: https://doi.org/10.1039/d3im00135k

© 2024 The Author(s). Co-published by the Institute of Process Engineering, Chinese Academy of Sciences and the Royal Society of Chemistry

Open Access Article. Published on 20 mis Hwevrer 2024. Downloaded on 08/01/2026 10:34:26.
This article is licensed under a Creative Commons Attribution-NonCommercial 3.0 Unported Licence.

superior water-splitting capabilities compared to their isolated counterparts.[22] This suggests that liquid water might serve as a more effective reactant source than water vapor for low-temperature WGS reaction. Notably, under standard conditions (25 °C, 1 atm), CO molecules demonstrate limited solubility (~1 mM) and a modest diffusion coefficient (2.03×10^{-5} cm^2 s^{-1}) in the aqueous phase.[23,24] This implies that in liquid–solid (L–S) diphase photocatalytic systems, which has been widely investigated for decades, the WGS reaction might be hindered by the interfacial mass transfer of CO molecules. Effectively enhancing both the mass transfer and the chemical reaction between gaseous CO and liquid H_2O at the photocatalytic interface presents a complex challenge.

Recently, the scientific community has delved into photocatalysis at gas–liquid–solid (G–L–S) triphase interfaces. This approach has demonstrated distinct advantages in various photocatalytic reactions involving both gas and water reactants, such as CO_2 reduction, active oxygen generation, and ethylene purification.[25–27] By facilitating the diffusion of CO and H_2O to the photocatalyst surface *via* both gaseous and liquid phases, the WGS reaction at G–L–S interfaces holds promise in overcoming the constraints observed in diphase systems, potentially enhancing the overall H_2 production efficiency under mild reaction conditions.

In this study, we introduce a triphase photocatalytic system tailored for the WGS reaction, leveraging metal-loaded TiO_2 (M/TiO_2, where M represents Rh, Au, Ag, Pt, and Pd) as the benchmark photocatalysts. To realize this setup, a hydrophobic porous layer served as the support, enabling the photocatalysts to float at the gas–water interface and fostering abundant G–L–S interfaces. Among tested photocatalysts, Rh/TiO_2 demonstrated the highest H_2 production rate of 27.60 mmol g^{-1} h^{-1}. Remarkably, this rate surpasses that of both the corresponding L–S and G–S diphase systems by factors of approximately 2 and 10, respectively. Finite element simulations reveal consistent concentrations of CO and H_2O at the G–L–S interface during the photocatalytic diffusion–reaction process, although a significant decline in CO is evident at the L–S interface. This observation aligns with the elevated H_2 production rates observed in the triphase system when utilizing diluted CO (0.02 MPa) as the gaseous feedstock. Serving as a proof-of-concept, our results underscore the pivotal role of the G–L–S triphase interface in augmenting the interfacial mass transfer and reaction of gaseous CO and liquid H_2O, thereby enhancing the efficiency of the photocatalytic WGS reaction.

2 Results and discussion

The structural characteristics and surface morphology of the Rh/TiO_2 photocatalysts were systematically examined, as depicted in Fig. 1. The X-ray diffraction (XRD) profile of *x* wt% Rh/TiO_2 (*x* = 1, 3, 5, 7, and 9) reveals the presence of both anatase TiO_2 (JCPDS no. 73-1764) and rutile TiO_2 (JCPDS no. 87-0710). Notably, no discernible signal corresponding to metallic Rh was observed across all Rh/TiO_2 samples (Fig. 1a). This absence could be attributed to the small crystal dimensions and the relatively modest Rh content.[28] The

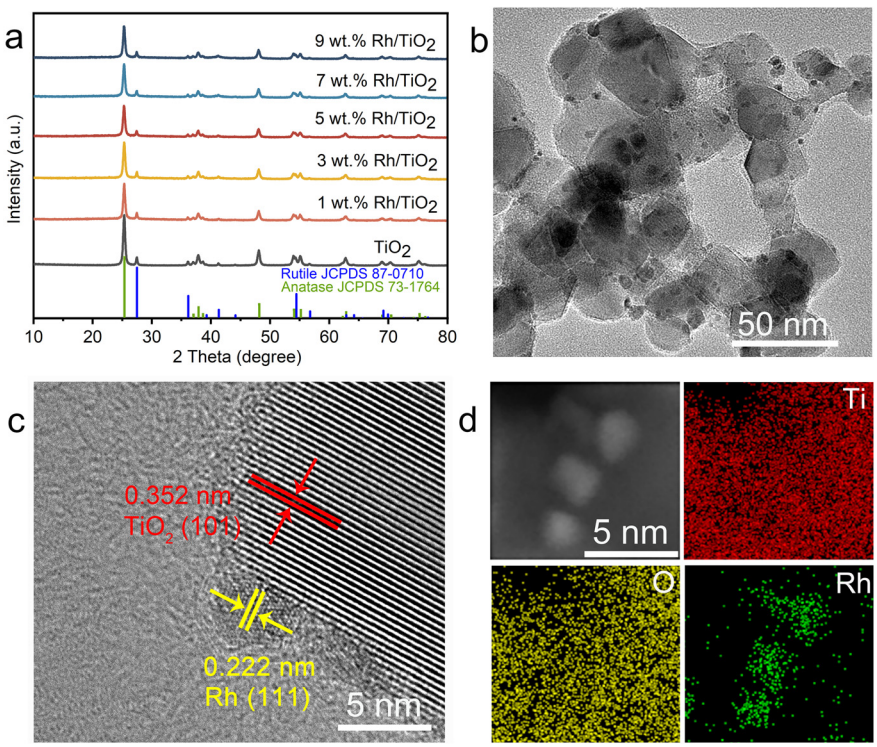

Fig. 1 Characterization for Rh/TiO_2 photocatalysts. (a) XRD pattern for *x* wt% Rh/TiO_2; (b) TEM image and (c) high-resolution TEM image of 5 wt% Rh/TiO_2; (d) the HAADF-STEM image and EDS element maps of 5 wt% Rh/TiO_2.

© 2024 The Author(s). Co-published by the Institute of Process Engineering, Chinese Academy of Sciences and the Royal Society of Chemistry

Open Access Article. Published on 20 mis Hwevrer 2024. Downloaded on 08/01/2026 10:34:26.
This article is licensed under a Creative Commons Attribution-NonCommercial 3.0 Unported Licence.

experimental loading content of Rh within TiO_2 align closely with the theoretical values (Fig. S1†). 5 wt% Rh/TiO_2 was utilized throughout unless otherwise stated. Upon examination *via* transmission electron microscopy (TEM) and high-resolution TEM, Rh nanoparticles, each having a diameter of approximately 2.0 ± 0.5 nm, were found to be uniformly dispersed over the TiO_2 surface (Fig. 1b and S2†). The observed lattice spacings of 0.352 nm and 0.222 nm correspond to the *d*-spacing values of TiO_2 (101) and Rh (111), respectively (Fig. 1c). Moreover, high-angle annular dark-field scanning TEM (HAADF-STEM) coupled with energy-dispersive X-ray spectroscopy (EDS) elemental mapping corroborates the distinct spatial distribution of Rh nanoparticles on TiO_2 (Fig. 1d).

Polytetrafluoroethylene gas diffusion layers (GDL) served as the porous substrates for the immobilization of the photocatalyst. Rh/TiO_2 was anchored onto the GDL using a vacuum filtration method, denoted as Rh/TiO_2-GDL. The structure of Rh/TiO_2-GDL is evident in the cross-sectional scanning electron microscopy (SEM) image presented in Fig. 2a. The corresponding EDS mapping, highlighting Ti, C, and F elements, provides insights into the photocatalyst layer's thickness, which is approximately 1.4 ± 0.2 μm (Fig. 2b). The top-view SEM reveals a distinct cross-linked fibre network within the porous substrate, establishing abundant pores for efficient gas diffusion (Fig. 2c). The inset of Fig. 2c displays a water droplet contact angle of 126°, underscoring the inherent hydrophobic nature of the GDL porous substrate. After the immobilization of Rh/TiO_2, the resultant photocatalyst layer exhibits a significantly reduced water contact angle of 19°, indicating a pronounced hydrophilic–hydrophobic transition within the Rh/TiO_2-GDL layered structure (Fig. 2d).

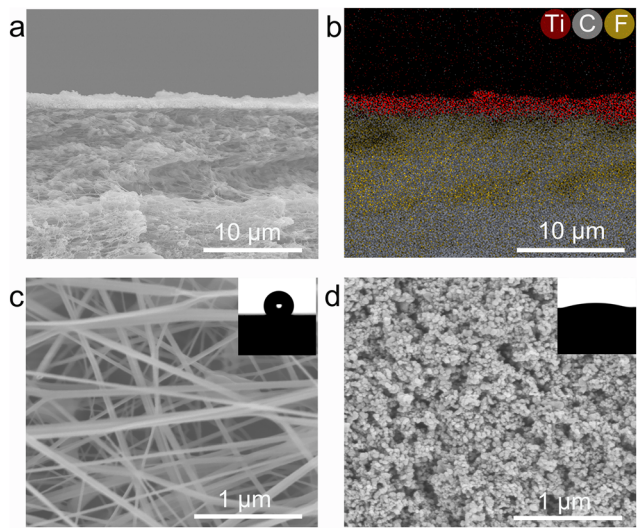

Fig. 2 Structural characterization of the Rh/TiO_2-GDL. (a) Cross-sectional SEM image and (b) corresponding EDS mapping of Rh/TiO_2-GDL; top-view SEM images of (c) pristine GDL porous substrate and (d) immobilized Rh/TiO_2 photocatalyst layer. Inserts in (c) and (d) show photographs of water droplets on each sample.

As illustrated in Fig. 3a, both pristine TiO_2 and all *x* wt% Rh/TiO_2 samples exhibit pronounced absorption in the ultraviolet region, attributed to the characteristic edge adsorption of TiO_2. The visible light absorption, corresponding to Rh nanoparticles, amplifies with increasing Rh loading. To further discern the influence of different metal species on the WGS reaction, other M/TiO_2 (where M = Au, Ag, Pt, and Pd) with a consistent metal loading of 5 wt% were synthesized using analogous procedures. The XRD patterns exhibit characteristic peaks corresponding to anatase TiO_2 (JCPDS no. 73-1764) and rutile TiO_2 (JCPDS no. 87-0710), while characteristic peaks corresponding to metal are notably absent, possibly attributable to the small crystal dimensions (Fig. S3†). The TEM images confirm the successful loading of metal nanoparticles onto TiO_2 for all M/TiO_2 samples (Fig. S4†). The achieved metal content closely aligns with theoretical predictions (Fig. S5†), with all samples demonstrating robust optical absorption below 400 nm (Fig. S6†). Consequently, a 365 nm LED lamp was employed as the illumination source to assess the photocatalytic efficiency. The H_2 production rates of Rh/TiO_2 and the other M/TiO_2 photocatalysts in the G–L–S triphase system are depicted in Fig. 3b. TiO_2 modified with distinct metals showcases marked variations in H_2 production rates under both CO (WGS) and Ar (pure water splitting) gas phase conditions. In an Ar environment, Pt/TiO_2 achieves the highest H_2 production rate of 5.95 mmol g^{-1} h^{-1}, consistent with prior studies employing Pt as co-catalysts for photocatalytic water splitting.[29–31] However, transitioning to a CO environment only results in a slight enhancement over Pt/TiO_2, suggesting a minimal contribution of the WGS reaction to H_2 generation. Conversely, Rh/TiO_2 registers a five-fold enhancement in H_2 production rate (25.77 mmol g^{-1} h^{-1}) compared to its performance in an Ar condition, underscoring the pivotal role of CO in enhancing generating H_2 *via* the WGS pathway. A pronounced boost was also observed for Au/TiO_2 (13.77 mmol g^{-1} h^{-1}), with the H_2 production trend across M/TiO_2 as follows: Rh/TiO_2 > Au/TiO_2 > Pt/TiO_2 > Ag/TiO_2 > Pd/TiO_2. The observed disparities in H_2 production rates among various M/TiO_2 samples in different gas conditions likely stem from the synergistic interplay between CO adsorption and proton reduction kinetics at the metal active sites.[32,33]

The loading amount of Rh within Rh/TiO_2 significantly impacts its photocatalytic WGS efficiency. As depicted in Fig. 3c, the H_2 production rate escalates progressively from 15.10 to 28.17 mmol g^{-1} h^{-1} with Rh loadings escalating from 1 wt% to 5 wt%. However, augmenting the Rh content beyond 5 wt% only marginally enhances the H_2 production rate. Consequently, 5 wt% Rh-loaded Rh/TiO_2 was adopted for subsequent experiments. Subsequently, a photostability assessment was conducted on Rh/TiO_2 within the G–L–S photocatalytic system. Under continuous irradiation for 5 hours, the H_2 production rate shows a linear correlation with irradiation time, culminating in a cumulative yield of 111.52 mmol g^{-1} (Fig. S7†). Additionally, Fig. 3d underscores that

© 2024 The Author(s). Co-published by the Institute of Process Engineering, Chinese Academy of Sciences and the Royal Society of Chemistry

Open Access Article. Published on 20 mis Hwevrer 2024. Downloaded on 08/01/2026 10:34:26.
This article is licensed under a Creative Commons Attribution-NonCommercial 3.0 Unported Licence.

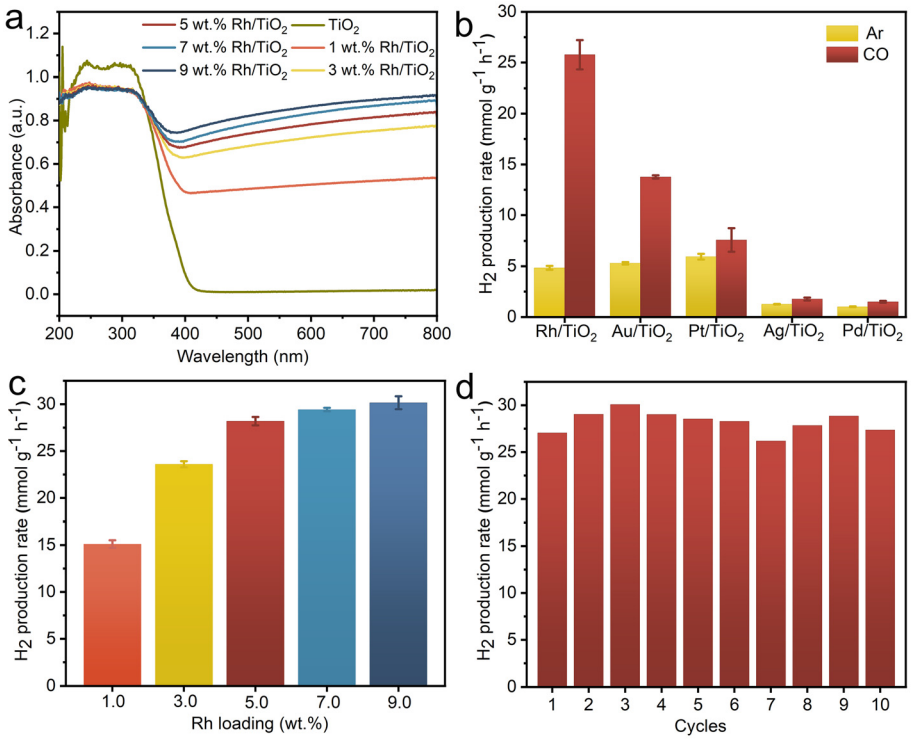

Fig. 3 (a) Absorption spectra for TiO_2 and *x* wt% Rh/TiO_2; (b) triphase photocatalytic H_2 production rate for 5 wt% M/TiO_2 (M = Rh, Au, Ag, Pt, Pd) in Ar or CO atmosphere; (c) photocatalytic H_2 production rate as a function of the loading amount of Rh in Rh/TiO_2; (d) cycling tests for Rh/TiO_2. Reaction conditions: gas phase = 0.2 MPa of CO, liquid phase = 10 mL of H_2O, solid phase = 2 mg of photocatalyst immobilized on GDL (4 cm in diameter), light source = 365 nm LED (300 mW cm^{-2}). Error bars represent the standard deviation from at least three independent measurements.

the H_2 production activity of the Rh/TiO_2 photocatalyst remains consistent after 10 photocatalytic cycles (1 h for each cycle, 10 h in total). Notably, the structure and morphology of the Rh/TiO_2 photocatalyst show no obvious change after the

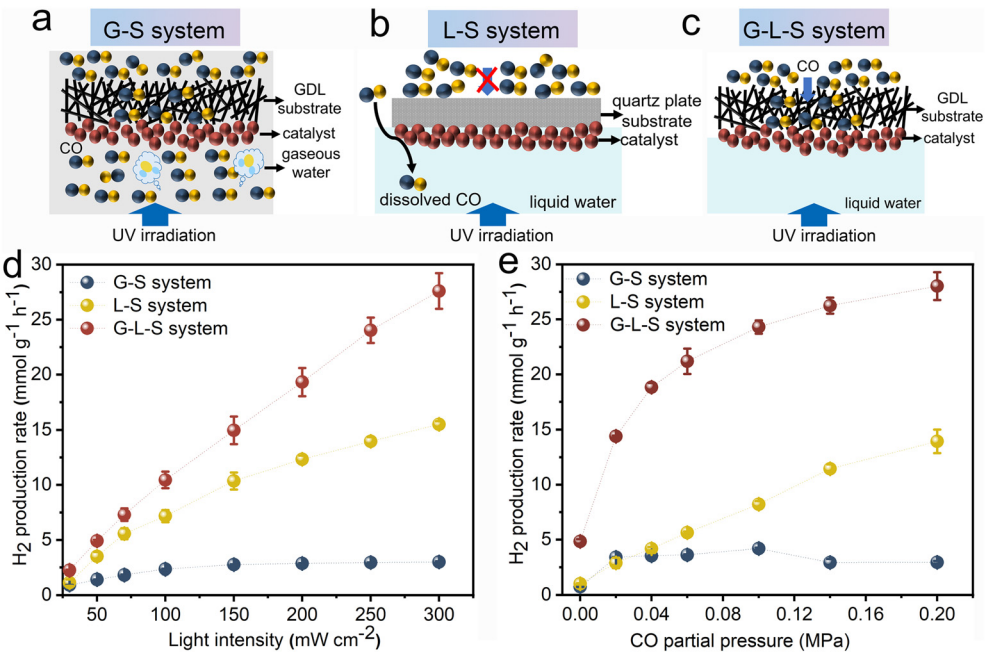

Fig. 4 Schematic illustration of (a) G–S, (b) L–S, and (c) G–L–S systems; (d) light intensity-dependent photocatalytic H_2 production rate over Rh/TiO_2 at a CO partial pressure of 0.2 MPa; (e) CO partial pressure-dependent photocatalytic H_2 production rate at a light intensity of 300 mW cm^{-2}. Error bars represent the standard deviation from at least three independent measurements.

© 2024 The Author(s). Co-published by the Institute of Process Engineering, Chinese Academy of Sciences and the Royal Society of Chemistry

Open Access Article. Published on 20 mis Hwevrer 2024. Downloaded on 08/01/2026 10:34:26.
This article is licensed under a Creative Commons Attribution-NonCommercial 3.0 Unported Licence.

cycling test (Fig. S8 and S9†), signify its commendable photostability. The contact angle of water droplets on the GDL porous substrate did not show a significant change after the cycling experiment (Fig. S10†), indicating its stable hydrophobicity.

The photocatalytic WGS reaction was examined across various triphase and diphase systems using Rh/TiO_2 as the photocatalyst. Schematic illustrations of the G–S and L–S diphase system and the G–L–S triphase system are provided in Fig. 4a–c. For the G–S system (Fig. 4a), which is a configuration frequently employed in conventional (photo) thermal WGS reactions, the CO reactant can directly diffuse to the photocatalyst from the gas phase. The water concentration within this gas phase is standardized at 0.95 mM, representing 74% of the relative humidity at room temperature. Fig. 4b showcases the L–S system where Rh/TiO_2 is immobilized onto a quartz plate instead of the GDL porous substrate. Here, CO from the gas phase dissolves and undergoes a long-range diffusion process within the aqueous phase to reach the photocatalyst. In the G–L–S system, as depicted in Fig. 4c, gaseous CO traverses to the photocatalyst's surface *via* the hydrophobic GDL pores. Simultaneously, a high interfacial water concentration (equivalent to 55.6 M for pure water) is maintained at ambient conditions. This ensures an optimized diffusion–reaction process for both CO and H_2O molecules during the photocatalytic WGS reaction.

The photocatalytic WGS reaction activities across the three systems were investigated using light intensity and CO partial pressure as variables. As depicted in Fig. 4d, the light intensity-dependent behaviour of the photocatalytic WGS reaction was evaluated at a constant CO partial pressure of 0.2 MPa. Within the G–S system, the WGS reaction performance remained largely insubstantial across the tested light intensities (30–300 mW cm^{-2}). This minimal activity could be attributed to certain limiting factors. In the L–S system, the H_2 production rate surged to 7.16 mmol g^{-1} h^{-1} at an intensity of 100 mW cm^{-2}, but only experienced a twofold increase upon elevating the intensity to 300 mW cm^{-2}. These findings imply that at higher light intensities, the rate-determining step potentially shifts to the mass transfer of CO, given the rapid depletion of reactants. Conversely, within the G–L–S system, the H_2 production rate exhibited a nearly linear augmentation even under elevated light intensities. This behaviour suggests that the rate-limiting steps are more associated with the photo-generation and subsequent separation of charge carriers, rather than the mass transfer process. Notably, the H_2 production rate within the triphase system reached 27.60 mmol g^{-1} h^{-1} at 300 mW cm^{-2}, marking an approximately twofold and tenfold enhancement compared to the L–S and G–S diphase systems, respectively.

Subsequently, the impact of CO partial pressure on the photocatalytic WGS reaction was assessed with a consistent light intensity set at 300 mW cm^{-2}, as illustrated in Fig. 4e. In the G–S system, escalating CO partial pressures did not yield any discernible increase in activity, aligning with prior observations. In contrast, the L–S system showcased a nearly proportional correlation between the H_2 production rate and CO partial pressure, peaking at 13.93 mmol g^{-1} h^{-1} at 0.2 MPa. These findings indicate an increased solubility of CO molecules in the aqueous phase and an enhanced mass transfer, both of which correlate positively with elevated CO partial pressures in the connected gas phase. Within the G–L–S system, the H_2 production rate witnessed a marked surge at modest CO partial pressures, outperforming the L–S system at a 10 times reduced CO partial pressure of 0.02 MPa (14.37 mmol g^{-1} h^{-1}). This underscores the G–L–S system's advantage in selectively converting low-concentration CO, positioning potential applications like CO removal in fuel cells (for hydrogen purification) and mitigating CO poisoning risks in confined environments. However, the rate of enhancement decelerates at elevated CO partial pressures, indicative of a transition in the rate-determining step, potentially shifting from CO mass transfer to other processes, such as the photo-generation and subsequent separation of charge carriers.

A three-dimensional finite element method (FEM) simulation was employed to computationally elucidate the interfacial mass transfer of CO and H_2O across various reaction systems. As depicted in the left panel of Fig. 5, three distinct models were constructed to represent the G–S (top), L–S (middle), and G–L–S (bottom) systems. In the G–L system, the simulation focused on the local H_2O concentration, with an initial concentration set at 0.95 mM based on experimental data. For both the L–S and G–L–S systems, the simulation targeted the local CO concentration, with the initial concentration determined by the saturated solubility of CO within the aqueous phase (1.01 mM).[23] The FEM simulation aimed to capture the diffusion–reaction dynamic process occurring at the reaction interface. To align with the optimized photocatalytic H_2 production rates observed in the G–L–S system (approximately 10 mM s^{-1}), the consumption rates of CO and H_2O within the photocatalytic layer region were modulated, ranging from 5 to 15 mM s^{-1}.

The *xz* diagrams depicting the simulated reactant concentrations for the G–S, L–S, and G–L–S systems are illustrated in Fig. 5a–c, respectively. In the G–S system (Fig. 5a), the local water vapor concentration within the photocatalyst layer exhibits minimal decline even at escalated H_2O consumption rates. This observation implies that the subdued H_2 production in the G–S setup might not be directly attributable to interfacial diffusion or mass transfer challenges of water molecules. Instead, it could be linked to the adverse impact of water vapor, characterized by a weak hydrogen bond network, on H_2 production, as previously suggested.[22] In the L–S system (Fig. 5b), where the photocatalyst layer is submerged within a bulk water phase, the local CO concentration surrounding the catalyst surface diminishes markedly with the rising CO consumption rate. However, the G–L–S configuration (Fig. 5c) showcases a consistent CO concentration even at elevated consumption

© 2024 The Author(s). Co-published by the Institute of Process Engineering, Chinese Academy of Sciences and the Royal Society of Chemistry

Open Access Article. Published on 20 mis Hwevrer 2024. Downloaded on 08/01/2026 10:34:26.
This article is licensed under a Creative Commons Attribution-NonCommercial 3.0 Unported Licence.

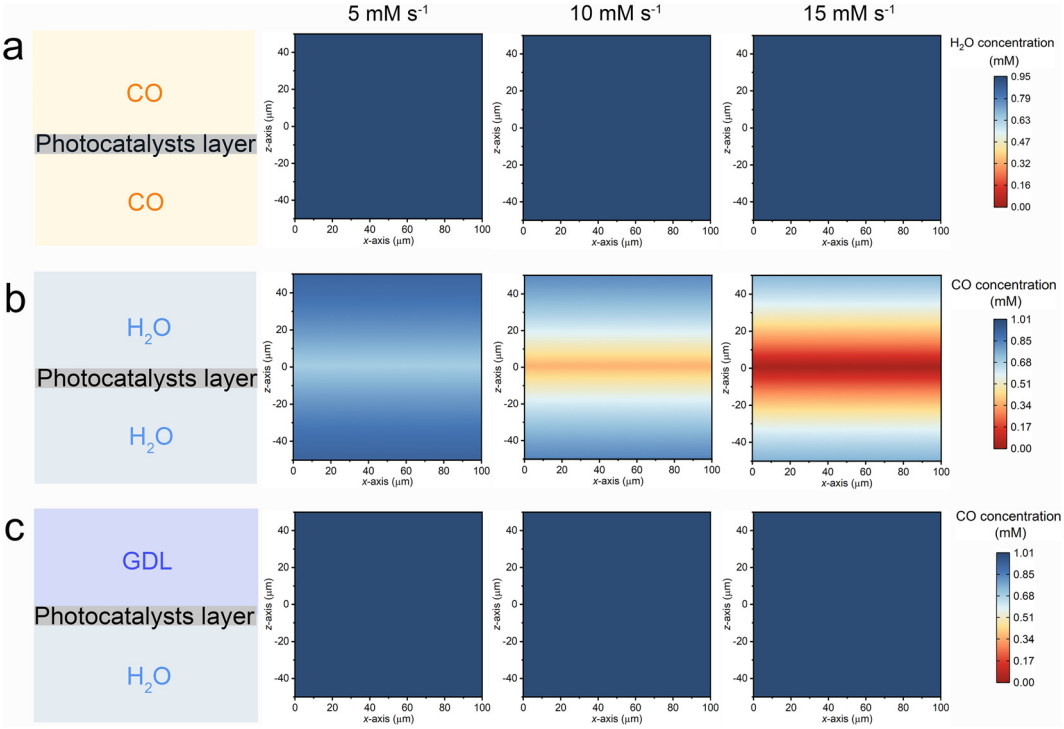

Fig. 5 Schematic diagrams and FEM simulation results of (a) G–S, (b) L–S, and (c) G–L–S systems. The colour scale in (a) represents the water vapor concentration, in (b) and (c) represents the CO concentration.

rates. This stability underscores the function of the triphase interface in maintaining a robust supply of CO molecules within the local reaction microenvironment. Such consistent CO availability ensures efficient H_2 production *via* the photocatalytic WGS pathway, even when subjected to diluted CO conditions.

3 Conclusions

In summary, we have developed a G–L–S triphase photocatalytic system utilizing M/TiO_2 (where M = Rh, Au, Ag, Pt, and Pd) immobilized on a hydrophobic porous GDL for the WGS reaction under ambient conditions. Among the tested catalysts, Rh/TiO_2 exhibited the most impressive photocatalytic H_2 production rate, registering at 27.60 mmol g^{-1} h^{-1}. This catalyst not only showcased commendable photostability but also displayed remarkable enhancements, even when utilizing gas sources with low CO concentrations. Crucially, the G–L–S configuration notably enhances the mass transfer of both CO and H_2O to the photocatalyst surface, which appears to be the primary rate-determining step. Consequently, this design exhibited H_2 production rates that were 10 and 2 times higher than those observed in conventional G–S and L–S diphase systems, respectively. FEM simulations provided insights into the interfacial mass transfer process of CO and H_2O. These findings underscore the triphase system's distinct advantage in ensuring a consistent CO supply to the photocatalyst layer, especially under low-concentration conditions. Overall, our research underscores the promising potential of the G–L–S triphase photocatalytic system, highlighting its capability to optimize the diffusion–reaction interplay in the WGS process, thereby achieving superior H_2 production efficiencies under mild conditions.

4 Experimental section

4.1 Chemicals and materials

TiO_2 (P25) was purchased from Degussa AG. $RhCl_3{\cdot}3H_2O$ was obtained from Bide Pharmatech Ltd. (China). $HAuCl_4{\cdot}4H_2O$, $H_2PtCl_6{\cdot}6H_2O$, and Na_2PdCl_4 were purchased from Aladdin (Shanghai, China). $AgNO_3$ was purchased from Sinopharm Chemical Reagent Corporation (Shanghai, China). $NaBH_4$ was purchased from Guangdong Guanghua Chemical Factory Co., Ltd. Polytetrafluoroethylene GDL with a thickness of 30 μm and a diameter of 47 mm (Chuangwei Filter Media, China) was used as a porous support for photocatalyst immobilization. All chemicals were analytically pure and had not been further purified. Deionized water was used in the whole experiments.

4.2 Photocatalyst preparation

Preparation of M/TiO_2: M/TiO_2 with varying weight loadings were synthesized using the $NaBH_4$ reduction method as described by Zhang.[34] Specifically, for the preparation of Rh/TiO_2, 200 mg of TiO_2 was dispersed in 100 mL of water using ultrasonication for 30 minutes. Subsequently, different volumes of an aqueous $RhCl_3{\cdot}3H_2O$ solution (with a

© 2024 The Author(s). Co-published by the Institute of Process Engineering, Chinese Academy of Sciences and the Royal Society of Chemistry

Open Access Article. Published on 20 mis Hwevrer 2024. Downloaded on 08/01/2026 10:34:26.
This article is licensed under a Creative Commons Attribution-NonCommercial 3.0 Unported Licence.

concentration of 10 mg mL^{-1} for Rh) were introduced to the aforementioned dispersion and sonicated for another 30 minutes. Following this, a surplus $NaBH_4$ solution (concentration: 2.5 mg mL^{-1}) was meticulously added dropwise to the suspension with continuous stirring. After an additional hour of stirring, the samples underwent centrifugation, followed by rinsing with neutral water. They were then subjected to overnight vacuum freeze-drying. The resulting catalysts were denoted as x wt% Rh/TiO_2 (x = 1, 3, 5, 7, and 9, representing the theoretical weight ratio of Rh loadings). A consistent synthesis approach was adopted for other M/TiO_2 variants, employing appropriate aqueous solutions of $HAuCl_4{\cdot}4H_2O$, $AgNO_3$, $H_2PtCl_6{\cdot}6H_2O$, and Na_2PdCl_4 for the synthesis of Au/TiO_2, Ag/TiO_2, Pt/TiO_2, and Pd/TiO_2, respectively.

Preparation of M/TiO_2-GDL: taking Rh/TiO_2 as an example, the ethanol dispersion of Rh/TiO_2 (concentration: 0.1 mg mL^{-1}) was subjected to sonication for approximately 30 minutes. Subsequently, 20 mL of this suspension was applied to the GDL surface *via* vacuum filtration, resulting in a circular photocatalyst layer with a diameter of 4 cm. After a 1 hour drying period in an oven, Rh/TiO_2-GDL with a loading density of 0.16 mg cm^{-2} was obtained (Fig. S11a†). This layer was then utilized for both the G–L–S and G–S systems. For the L–S system, a 20 mL ethanol dispersion of Rh/TiO_2 (concentration: 0.1 mg mL^{-1}) was dripped onto the surface of a circular quartz substrate (4 cm in diameter), followed by a 1 hour drying process in an oven (Fig. S11b†).

4.3 Characterization

The structure and crystallization of the particles were provided by XRD (Bruker AXSD8 Advance, Germany). Sample morphologies were examined using SEM (S4800, Hitachi, Japan) and TEM (JEOL-2100F, Japan), both of which were equipped with EDS for elemental analysis. The diffuse reflection spectra of the photocatalyst powders were measured using an ultraviolet-visible spectrophotometer (Cary 7000, Agilent, USA) with an integrating sphere attachment. A contact angle system (OCA20, Dataphysics, Germany) was used to measure the contact angles, with the probe liquid being a 2.0 μL droplet of water.

4.4 Photocatalytic measurements

Photocatalytic WGS reaction measurements: The photocatalytic activities of the synthesized samples were evaluated using a custom-built photocatalytic reactor (Fig. S12 and S13†). A 365 nm LED (PLS-LED100C, PerfectLight, China), paired with a $\lambda < 400$ nm filter (Xujiang Electromechanical Plant, Nanjing, China), served as the illumination source. In the G–S configuration, the Rh/TiO_2-GDL was positioned within the reactor. CO (99.99%) was then bubbled through a water tank, producing a CO/water gas mixture under atmospheric conditions. The humidified CO was introduced into the reactor at a flow rate of 400 mL min^{-1} for 30 minutes, achieving a water vapor concentration of 0.95 mM (equivalent to 74% relative humidity). Subsequently, the reaction gas was introduced to elevate the pressure to 0.2 MPa. For the L–S system, the Rh/TiO_2-immobilized quartz plate was submerged in 10 mL of water. For the G–L–S system, the Rh/TiO_2-GDL was positioned above a 10 mL water surface. Both L–S and G–L–S systems were pressurized to 0.20 MPa with CO gas and then sealed. After a 1 hour irradiation period, the WGS reaction products were quantified using a gas chromatograph (GC-2014C, Shimadzu, Japan) equipped with a TCD detector, molecular sieve 5, and utilizing N_2 as the carrier gas. For the photocatalytic cycling stability experiment, reaction products were quantitatively analysed using a gas chromatograph after 1 hour of irradiation. Subsequently, the gas within the photocatalytic reactor was entirely exhausted and replaced with CO for the subsequent cycle. This cycle was repeated ten times.

Light intensity and CO partial pressure modulation: Experiments were conducted to assess the light intensity dependence in the photocatalytic WGS reaction, maintaining a constant CO partial pressure of 0.2 MPa. The varying light intensities were achieved by modulating the output power of the 365 nm LED. Additionally, tests at different CO partial pressures were performed under a steady light intensity of 300 mW cm^{-2}. The CO partial pressures were adjusted by manipulating the CO/Ar volume ratio at a consistent total pressure of 0.2 MPa.

4.5 FEM simulation

The mass transfer and consumption behaviours of CO and H_2O in the G–S, L–S, and G–L–S systems were analysed *via* Fick's second law using FEM simulations conducted in COMSOL 5.4. Fick's second law is as follows:

$$\frac{\partial C_i}{\partial t} + \nabla{\cdot}\boldsymbol{J}_i + u{\cdot}\nabla C_i = R_i \quad (1)$$

$$\boldsymbol{J}_i = -D_i \nabla C_i, u = \frac{x}{\sqrt{t}} \quad (2)$$

C_i is the concentration of dimensions, t is the time, D_i is the diffusion coefficient in dimensions, ∇C_i is the Laplacian, and x is the distance. The three-dimensional geometric models of these systems were 500 μm × 500 μm × 400 μm (Fig. S14†). In the G–S system, the sequence from top to bottom comprises the gas phase, the photocatalyst layer, and the gas phase. The water vapor concentrations on both the upper and lower surfaces were set to 0.95 mM. The L–S system was structured with the liquid phase sandwiching the photocatalyst layer. The CO concentrations on both the upper and lower surfaces were set to 1.01 mM, representing the CO solubility saturation in aqueous solutions under standard conditions (25 °C, 1 atm).[23] In the G–L–S system, a sequence was established from top to bottom: the gas diffusion layer, photocatalyst layer, and the liquid phase. CO concentrations of 1.01 mM in aqueous solutions were applied to both upper and lower surfaces. For all models, the diffusion constant of water vapor in the gas phase was set as 1.3×10^{-5} m^2 s^{-1},[24]

© 2024 The Author(s). Co-published by the Institute of Process Engineering, Chinese Academy of Sciences and the Royal Society of Chemistry

Open Access Article. Published on 20 mis Hwevrer 2024. Downloaded on 08/01/2026 10:34:26.
This article is licensed under a Creative Commons Attribution-NonCommercial 3.0 Unported Licence.

while the diffusion constants of CO were set as follows: 2.2×10^{-5} m^2 s^{-1} in the gas phase, 2.03×10^{-9} m^2 s^{-1} in the aqueous phase, and 2.4×10^{-6} m^2 s^{-1} in the gas diffusion layer.[34–36]

Conflicts of interest

The authors declare no conflict of interest.

Acknowledgements

The authors are grateful for financial support from the National Key R&D Program of China (2021YFA1500803), the National Natural Science Foundation of China (51825205, 52120105002, 22272190, 22209190, 22088102), the Beijing Natural Science Foundation (2222035), the CAS Project for Young Scientists in Basic Research (YSBR-004), the DNL Cooperation Fund, CAS (DNL202016), the China Postdoctoral Science Foundation (2021M703288, 2021T150665), the Young Elite Scientist Sponsorship Program by CAST (2021QNRC001), and the Youth Innovation Promotion Association of the CAS.

References

1 M. G. Rasul, M. A. Hazrat, M. A. Sattar, M. I. Jahirul and M. J. Shearer, The future of hydrogen: Challenges on production, storage and applications, *Energy Convers. Manage.*, 2022, **272**, 116326.
2 W. H. Chen and C. Y. Chen, Water gas shift reaction for hydrogen production and carbon dioxide capture: A review, *Appl. Energy*, 2020, **258**, 114078.
3 K. Ayers, N. Danilovic, R. Ouimet, M. Carmo, B. Pivovar and M. Bornstein, Perspectives on low-temperature electrolysis and potential for renewable hydrogen at scale, *Annu. Rev. Chem. Biomol. Eng.*, 2019, **10**, 219–239.
4 R. M. Navarro, M. A. Peña and J. L. G. Fierro, Hydrogen production reactions from carbon feedstocks fossil fules and biomass, *Chem. Rev.*, 2007, **107**, 3952–3991.
5 J. D. Holladay, J. Hu, D. L. King and Y. Wang, An overview of hydrogen production technologies, *Catal. Today*, 2009, **139**, 244–260.
6 C. Ratnasamy and J. P. Wagner, Water gas shift catalysis, *Catal. Rev.: Sci. Eng.*, 2009, **51**, 325–440.
7 A. Ambrosi and S. E. Denmark, Harnessing the power of the water-gas shift reaction for organic synthesis, *Angew. Chem., Int. Ed.*, 2016, **55**, 12164–12189.
8 Y. X. Tong, L. Z. Song, S. B. Ning, S. X. Ouyang and J. H. Ye, Photocarriers-enhanced photothermocatalysis of water-gas shift reaction under H_2-rich and low-temperature condition over $CeO_2/Cu_{1.5}Mn_{1.5}O_4$ catalyst, *Appl. Catal., B*, 2021, **298**, 120551.
9 S. Y. Yao, X. Zhang, W. Zhou, R. Gao, W. Q. Xu, Y. F. Ye, L. L. Lin, X. D. Wen, P. Liu, B. B. Chen, E. Crumlin, J. G. Guo, Z. J. Zuo, W. Z. Li, J. L. Xie, I. Lu, C. Kiely, L. Gu, G. Shi, J. Rodriguez and D. Ma, Atomic-layered Au clusters on α-MoC as catalysts for the low-temperature water-gas shift reaction, *Science*, 2017, **357**, 389–393.
10 Z. H. Zhang, X. Y. Chen, J. C. Kang, Z. Y. Yu, J. Tian, Z. M. Gong, A. P. Jia, R. You, K. Qian, S. He, B. T. Teng, Y. Cui, Y. Wang, W. H. Zhang and W. X. Huang, The active sites of Cu-ZnO catalysts for water gas shift and CO hydrogenation reactions, *Nat. Commun.*, 2021, **12**, 4331.
11 K. Xu, C. Ma, H. Yan, H. Gu, W. W. Wang, S. Q. Li, Q. L. Meng, W. P. Shao, G. H. Ding, F. R. Wang and C. J. Jia, Catalytically efficient $Ni\text{-}NiO_x\text{-}Y_2O_3$ interface for medium temperature water-gas shift reaction, *Nat. Commun.*, 2022, **13**, 2443.
12 Z. H. Cui, S. Song, H. B. Liu, Y. T. Zhang, F. Gao, T. Ding, Y. Tian, X. B. Fan and X. G. Li, Synergistic effect of Cu^+ single atoms and Cu nanoparticles supported on alumina boosting water-gas shift reaction, *Appl. Catal., B*, 2022, **313**, 121468.
13 Z. H. Zhang, S. S. Wang, R. Song, T. Cao, L. F. Luo, X. Y. Chen, Y. X. Gao, J. Q. Lu, W. X. Li and W. X. Huang, The most active Cu facet for low-temperature water gas shift reaction, *Nat. Commun.*, 2017, **8**, 488.
14 Y. J. Zhang, C. Q. Chen, X. Y. Lin, D. L. Li, X. H. Chen, Y. Y. Zhan and Q. Zheng, CuO/ZrO_2 catalysts for water-gas shift reaction: Nature of catalytically active copper species, *Int. J. Hydrogen Energy*, 2014, **39**, 3746–3754.
15 J. L. Santos, T. R. Reina, S. Ivanova, M. A. Centeno and J. A. Odriozola, Gold promoted $Cu/ZnO/Al_2O_3$ catalysts prepared from hydrotalcite precursors: Advanced materials for the WGS reaction, *Appl. Catal., B*, 2017, **201**, 310–317.
16 L. Torrente-Murciano and F. R. Garcia-Garcia, Effect of nanostructured support on the WGSR activity of Pt/CeO_2 catalysts, *Catal. Commun.*, 2015, **71**, 1–6.
17 A. Kubacka, M. Fernandez-García and G. Colón, Advanced nanoarchitectures for solar photocatalytic applications, *Chem. Rev.*, 2012, **112**, 1555–1614.
18 Y. Ma, X. L. Wang, Y. S. Jia, X. B. Chen, H. X. Han and C. Li, Titanium dioxide-based nanomaterials for photocatalytic fuel generations, *Chem. Rev.*, 2014, **114**, 9987–10043.
19 L. K. Zhao, Y. H. Qi, L. Z. Song, S. B. Ning, S. X. Ouyang, H. Xu and J. H. Ye, Solar-driven water-gas shift reaction over CuO_x/Al_2O_3 with 1.1% of light-to-energy storage, *Angew. Chem., Int. Ed.*, 2019, **58**, 7708–7712.
20 F. Sastre, M. Oteri, A. Corma and H. García, Photocatalytic water gas shift using visible or simulated solar light for the efficient, room-temperature hydrogen generation, *Energy Environ. Sci.*, 2013, **6**, 2211–2215.
21 N. Liu, M. Xu, Y. S. Yang, S. M. Zhang, J. Zhang, W. L. Wang, L. R. Zheng, S. Hong and M. Wei, $Au^{\delta-}$-Ov-Ti^{3+} interfacial site: catalytic active center toward low-temperature water gas shift reaction, *ACS Catal.*, 2019, **9**, 2707–2717.
22 X. C. Ma, Y. L. Shi, J. Y. Liu, X. T. Li, X. F. Cui, S. J. Tan, J. Zhao and B. Wang, Hydrogen-bond network promotes water splitting on the TiO_2 surface, *J. Am. Chem. Soc.*, 2022, **144**, 13565–13573.
23 K. S. Davidge, R. Motterlini, B. E. Mann, J. L. Wilson and R. K. Poole, Carbon monoxide in biology and microbiology: Surprising roles for the "detroit perfume", *Adv. Microb. Physiol.*, 2009, **56**, 85–167.

© 2024 The Author(s). Co-published by the Institute of Process Engineering, Chinese Academy of Sciences and the Royal Society of Chemistry

Open Access Article. Published on 20 mis Hwevrer 2024. Downloaded on 08/01/2026 10:34:26.
This article is licensed under a Creative Commons Attribution-NonCommercial 3.0 Unported Licence.

24 E. L. Cussler, *Diffusion: Mass Transfer in Fluid Systems*, Cambridge university press, Cambridge, 3rd edn, 2009.
25 H. N. Huang, R. Shi, Z. H. Li, J. Q. Zhao, C. L. Su and T. R. Zhang, Triphase photocatalytic CO_2 reduction over silver-decorated titanium oxide at a gas-water boundary, *Angew. Chem., Int. Ed.*, 2022, e202200802.
26 X. Y. Xiong, Z. P. Wang, Y. Zhang, Z. H. Li, R. Shi and T. R. Zhang, Wettability controlled photocatalytic reactive oxygen generation and Klebsiella pneumoniae inactivation over triphase systems, *Appl. Catal., B*, 2020, **264**, 118518.
27 L. J. Li, L. P. Xu, Z. F. Hu and J. C. Yu, Enhanced mass transfer of oxygen through a gas-liquid-solid interface for photocatalytic hydrogen peroxide production, *Adv. Funct. Mater.*, 2021, **31**, 2106120.
28 H. Song, X. G. Meng, Z. J. Wang, Z. Wang, H. L. Chen, Y. X. Weng, F. Ichihara, M. Oshikiri, T. Kako and J. H. Ye, Visible-light-mediated methane activation for steam methane reforming under mild conditions: A case study of Rh/TiO_2 catalysts, *ACS Catal.*, 2018, **8**, 7556–7565.
29 Y. J. Chen, S. F. Ji, W. M. Sun, Y. P. Lei, Q. C. Wang, A. Li, W. X. Chen, G. Zhou, Z. D. Zhang, Y. Wang, L. R. Zheng, Q. H. Zhang, L. Gu, X. D. Han, D. S. Wang and Y. D. Li, Engineeringthe atomic interface with single platinum atoms for enhanced photocatalytic hydrogen production, *Angew. Chem., Int. Ed.*, 2020, **59**, 1295–1301.
30 Y. L. Chen, X. Q. Liu, L. Hou, X. R. Guo, R. W. Fu and J. M. Sun, Construction of covalent bonding oxygen-doped carbon nitride/graphitic carbon nitride Z-scheme heterojunction for enhanced visible-light-driven H_2 evolution, *Chem. Eng. J.*, 2020, **383**, 123132.
31 C. C. Han, P. F. Su, B. H. Tan, X. G. Ma, H. Lv, C. Y. Huang, P. Wang, Z. F. Tong, G. Li, Y. Z. Huang and Z. F. Liu, Defective ultra-thin two-dimensional $g\text{-}C_3N_4$ photocatalyst for enhanced photocatalytic H_2 evolution activity, *J. Colloid Interface Sci.*, 2021, **581**, 159–166.
32 H. F. Wei, H. Liu, L. Yu, M. Zhang, Y. L. Zhang, J. C. Fan, X. J. Cui and D. H. Deng, Alloying Pd with Cu boosts hydrogen production via room-temperature electrochemical water-gas shift reaction, *Nano Energy*, 2022, **102**, 107704.
33 X. Zhang, M. T. Zhang, Y. C. Deng, M. Q. Xu, L. Artiglia, W. Wen, R. Gao, B. B. Chen, S. Y. Yao, X. C. Zhang, M. Peng, J. Yan, A. W. Li, Z. Jiang, X. Y. Gao, S. F. Cao, C. Yang, A. J. Kropf, J. N. Shi, J. L. Xie, M. S. Bi, J. A. van Bokhoven, Y. W. Li, X. D. Wen, M. Flytzani-Stephanopoulos, C. Shi, W. Zhou and D. Ma, A stable low-temperature H_2-production catalyst by crowding Pt on alpha-MoC, *Nature*, 2021, **589**, 396–401.
34 P. Wang, J. Q. Zhao, R. Shi, X. R. Zhang, X. D. Guo, Q. Dai and T. R. Zhang, Efficient photocatalytic aerobic oxidation of bisphenol A via gas-liquid-solid triphase interfaces, *Mater. Today Energy*, 2022, **23**, 100908.
35 I. Amdur and L. M. Shuler, Diffusion coefficients of the systems CO-CO and $CO\text{-}N_2$, *J. Chem. Phys.*, 1963, **38**, 188–192.
36 D. H. Shou, J. T. Fan, M. F. Mei and F. Ding, An analytical model for gas diffusion though nanoscale and microscale fibrous media, *Microfluid. Nanofluid.*, 2014, **16**, 381–389.

© 2024 The Author(s). Co-published by the Institute of Process Engineering, Chinese Academy of Sciences and the Royal Society of Chemistry